

Numerical Simulations on Drag Reduction Mechanism by Microbubbles

Kazuyasu, SUGIYAMA*, Takafumi KAWAMURA**, Shu TAKAGI*** and Yoichiro MATSUMOTO****

**Ship Performance Division, National Maritime Research Institute*

6-38-1, Shinkawa, Mitaka-shi, Tokyo, 181-0004, JAPAN

***Department of Environmental and Ocean Engineering, The University of Tokyo*

7-3-1 Hongo, Bunkyo-ku, Tokyo, 113-8656, JAPAN

****Department of Mechanical Engineering, The University of Tokyo*

7-3-1 Hongo, Bunkyo-ku, Tokyo, 113-8656, JAPAN

Numerical simulations are carried out in order to make clear the drag reduction mechanism by microbubbles. Some simulation methods are developed to consider effects such as the slip velocity on the bubble surface, the compressibility of the bubbly liquid, the density fluctuation and the bubble deformation and discuss these effects on the drag reduction by parametric studies.

1. Introduction

About 80% of the total propulsion resistance of a ship like a tanker is due to friction with the surrounding water. It will be a great contribution to the environment to reduce the fuel consumption of ships as a means of mass transportation by reducing the frictional drag. There are several devices for reducing the frictional resistance such as passive type devices like riblets or active type devices like the combination of micro sensors and actuators. Among these methods, we consider the microbubble injection method is most suitable for ships.

Over the last three decades, a lot of experiments have been performed on the microbubble drag reduction. McCormick and Bhattacharyya (1973) found the skin friction reduction of the submerged body by injecting the microbubbles produced by the electrolysis. The microbubble drag reduction has been also observed in the developing turbulent boundary layer flows on a flat plate (Bogdevich *et al.*, 1977; Madavan *et al.*, 1984; Pal *et al.*, 1988) and the fully developed turbulent channel flows (Guin *et al.*, 1996; Takahashi *et al.*, 1997; Kodama *et al.*, 2000). As they have reported, the efficiency of the microbubble drag reduction is positively correlated with the void fraction and reaches as much as 80%. For the industrial application of such the phenomena, it is important to make clear what is the governing factor for the drag reduction since a lot of factors are involved. However, experiments tend to be highly specialized and, consequently, measured correlation is often limited. Besides the presence of the microbubbles strongly hinders optical measurements.

Over the last two decades, some theoretical studies have been performed in order to explain the drag reduction mechanism. Legner (1984) proposed a simple model coupling with the mixing length model used in the turbulent boundary layer flow and the effective viscosity model for the liquid-gas mixture fluid. He concluded that there were three factors for the drag reduction, corresponding to the decrease of the Reynolds stress due to the decrease of the density, the increase of the effective viscosity due to the increase of the void fraction and the turbulent modulation by the bubble-water interaction. Madavan *et al.* (1985), Marie (1987) and Yoshida *et al.* (1997) have proposed similar models and predicted the drag reduction. However, such the models are too simple to make clear the drag reduction mechanism since the local interactions of the mass, the momentum and the energy between the liquid and gas phases are neglected.

With the recent development of computer performance, predicting fluid flows by numerical simulation is gaining popularity. Using the numerical simulations of the bubbly flow gives basic advantage of investigating the microbubble drag reduction because local interactions between the liquid and gas phases can be easily considered. Our objective is to elucidate the drag reduction mechanism, which is not yet clear, by numerical simulations. We develop some simulation methods to consider effects such as the slip velocity on the bubble surface, the compressibility of the bubbly liquid, the density fluctuation and the bubble deformation and discuss these effects on the drag reduction by parametric studies.

2. Effect of slip velocity on the bubble surface

In order to discuss the effect of the slip velocity on the bubble surface on the drag reduction, it is useful to compare

flows around undeformable spheres or cylinders between no-slip and free-slip boundary conditions. We have developed the simulation method for the no-slip boundary problem using a rectangular grid system (Sugiyama *et al.*, 2001). However, setting the free-slip boundary condition for a sphere or cylinder with the rectangular grid system, which is not fitted the boundary, has been numerically unstable. In the present study, we develop a new method for cylinders with the free-slip boundary using the rectangular grid system and carry out the numerical simulation of the Couett flows with cylindrical bubbles for both no-slip and free-slip boundary conditions.

2.1 Simulation method for free-slip boundary

In order to avoid numerical instability due to the representation of the free-slip boundary condition with the rectangular grid system, fluid flows on each grid point outside the cylinder are solved for the Navier-Stokes equation, while those inside the cylinder are based on the analytical solutions for the Stokes equation. The viscosity inside the cylinder is treated to be as much as that outside the cylinder. When expanding the velocity on the cylinder surface ($r=1$) as,

$$u_{j\theta}|_{r=1} = u_{\theta 0} + \sum_{n=1}^{\infty} \left[u_{\theta n}^{(c)} \cos n\theta + u_{\theta n}^{(s)} \sin n\theta \right], \quad (1)$$

the boundary conditions at $r=1$ are expressed as,

$$u_{pr} = 0, \quad u_{j\theta} = u_{j\theta}, \quad \frac{\partial(u_{j\theta}/r)}{\partial r} = 0. \quad (2)$$

The velocity inside the cylinder is given to satisfy the following solution with the free-slip boundary.

$$\begin{aligned} u_{pr} &= \frac{1}{4} \left(-u_{\theta 1}^{(s)} \cos \theta + u_{\theta 1}^{(c)} \sin \theta \right) (r^2 - r^{-2}) \\ &\quad + \sum_{n=2}^{\infty} \frac{n}{2(n-1)} \left(-u_{\theta n}^{(s)} \cos n\theta + u_{\theta n}^{(c)} \sin n\theta \right) (r^{n-1} - r^{-n+1}), \\ u_{j\theta} &= u_{\theta 0} r + \left(u_{\theta 1}^{(c)} \cos \theta + u_{\theta 1}^{(s)} \sin \theta \right) \left(\frac{3}{4} r^2 + \frac{1}{4} r^{-2} \right) \\ &\quad + \sum_{n=2}^{\infty} \left(u_{\theta n}^{(c)} \cos n\theta + u_{\theta n}^{(s)} \sin n\theta \right) \left(\frac{n}{2(n-1)} r^{n-1} + \frac{n-2}{2(n-1)} r^{-n+1} \right). \end{aligned} \quad (3)$$

2.2 Some general descriptions of numerical methods

The 2nd-order finite difference method is employed to solve the partial differential equations. The discretization of variables is carried out on the staggered grid. The time integral is evaluated using the 2nd order Adams-Bashforth method. In order to calculate $u_{\theta n}^{(c)}$ and $u_{\theta n}^{(s)}$, the cylinder surface is divided by 180 points and the velocity on them are interpolated by the 5th-order Lagrangian interpolation. The mode number for $\cos n\theta$ and $\sin n\theta$ is considered up to 10. The grid points per a cylinder radius is 10.

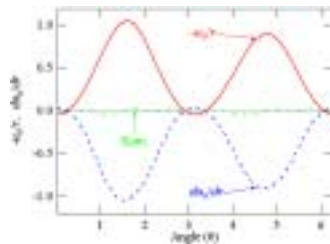


Fig. 1 Shear stress components on the cylinder surface

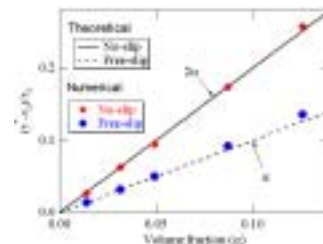


Fig. 2 Magnification ratio of the wall friction vs. void fraction

2.3 Validation of the present numerical method

In order to evaluate the validation of the present numerical method, the laminar Couette flow with free-slip cylinders is solved. Figure 1 shows the typical result of the shear stress components of $-u_{\theta} / r$ and $\partial u_{\theta} / \partial r$ on the cylinder surface obtained by the present numerical method. If the free-slip boundary condition is satisfied, their sum is to be zero. As shown in Fig. 1, the free-slip boundary condition is almost satisfied.

Figure 2 shows the magnification ratio of the wall friction ($(\tau^* - \tau_0) / \tau_0$) for various void fractions (α), where τ_0 represents the wall friction without cylinders and τ^* that with cylinders. The no-slip results are obtained by the method developed by Sugiyama *et al.* (2001). The Reynolds number scaled by the cylinder radius and the shear rate

is 0.1. At such the small Reynolds number, $(\tau^* - \tau_0)/\tau_0$ can be theoretically derived by the theory of the effective viscosity for suspension fluids (Batchelor, 1967), where the increase of the viscous dissipation due to the increase of the void fraction is considered. Theoretical solutions of $(\tau^* - \tau_0)/\tau_0$ for the no-slip and free-slip boundary conditions are equal to 2α and α , respectively. Lines and symbols in Fig. 2 correspond to theoretical and present numerical results, respectively. As shown in Fig. 2, the present numerical results show good agreement with the theoretical ones. From this result, the difference between the no-slip and free-slip condition can be captured by the present simulation method.

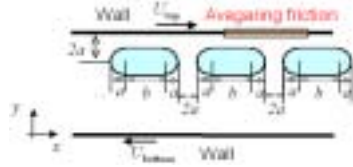


Fig. 3 Schematic figure of the present simulation

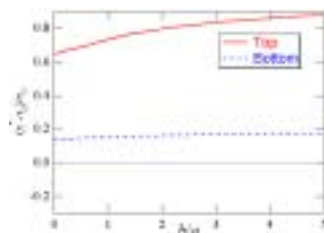


Fig. 4 Magnification ratio of the wall friction vs. b/a (No-slip bubble)

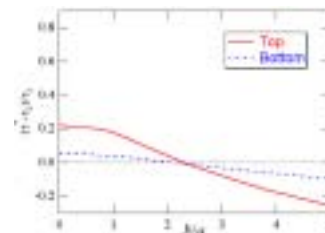


Fig. 5 Magnification ratio of the wall friction vs. b/a (Free-slip bubble)

2.4 Effect of the deformation of bubble

In order to investigate the effect of the bubble deformation on the drag reduction, the laminar Couette flow with flat bubbles is solved for various lengths of bubbles. The schematic figure shows in Fig. 3. Assuming the infinite flat bubble layer with the free-slip boundary is located, the force on the wall is 0. Thus, we can easily imagine the drag reduction will occur when the b in Fig. 3 is long enough. Figures 4 and 5 shows the relation between the magnification ratio of the wall friction $((\tau^* - \tau_0)/\tau_0)$ and b/a , corresponding to the results for the no-slip and free-slip bubbles, respectively. The Reynolds number scaled by a and the shear rate is 10. As shown in Fig. 4 for the no-slip bubble, $(\tau^* - \tau_0)/\tau_0$ becomes larger with the increase of b/a . It is because the flow space between the bubble and the wall becomes narrower with the increase of b/a . On the other hand, as shown in Fig. 5 for the free-slip bubble, $(\tau^* - \tau_0)/\tau_0$ becomes smaller with the increase of b/a . For the cylindrical bubble, the effective viscosity increases with the increase of the void fraction, which is influenced by the increase of the viscous dissipation due to the vorticity generation on the bubble surface. The vorticity is generated on the round region of the bubble surface, while it is not generated on the flat region. The decrease of the wall friction for the free-slip bubbles is resulted from the decrease of the vorticity generation. It is seen from Fig. 5 that the drag reduction occurs when the b/a is longer than 2.5. The present bubble aspect ratio for the onset of drag reduction is is much larger than that observed in the experiment (Takahashi *et al.*, 1997). Therefore, the drag reduction mechanism may be qualitatively explained by the deformation of the bubble, although it is necessary to involve the turbulence effect for quantitative discussions.

3. Effect of compressibility of bubbly liquid

It is wellknown that the sonic speed of the bubbly liquid quite goes down even in the low void fraction (Brennen, 1995). In the air/water system, the Mach number at the flow velocity of 15m/s is about 0.2 and 0.5 at the void fractions of 1% and 10%, respectively. According to the theoretical study on the inviscid stability of parallel bubbly flows (d'Agostino *et al.*, 1997), the bubble compressibility promotes the stability of the flow. Therefore, the compressibility of the bubbly liquid is considered to attenuate the turbulence intensity and alter the turbulence structure. In this section, the turbulent channel flow simulation is carried out to investigate whether the bubble compressibility affects the drag reduction or not.

3.1 Assumptions

In this study, the following assumptions are employed to formulate the governing equations.

- The bubble number density is constant.
- The bubbly liquid is homogeneous.
- Damping effect of the bubble radial motion is considered.
- The deviation of the pressure and the bubble radius from the initial values is small enough.

3.2 Governing equations

Mass conservation equation:

$$\frac{\partial \rho}{\partial t} + \nabla \cdot (\rho \mathbf{u}) = 0. \quad (4)$$

Momentum conservation equation:

$$\frac{\partial \rho \mathbf{u}}{\partial t} + \nabla \cdot (\rho \mathbf{u} \mathbf{u}) = -\nabla p + \mu \nabla \cdot \left((\nabla \mathbf{u}) + (\nabla \mathbf{u})^T - \frac{2}{3} (\nabla \cdot \mathbf{u}) \mathbf{I} \right) + \mathbf{H}. \quad (5)$$

Void fraction:

$$f_G = \frac{4}{3} \pi n_G R_G^3. \quad (6)$$

Relation between mixture density and void fraction:

$$\rho = (1 - f_G) \rho_L. \quad (7)$$

Relation between pressure and equilibrium radius of bubble:

$$p R_{GEQ}^3 = p_0 R_{GEQ0}^3. \quad (8)$$

Equation of bubble radial motion:

$$\frac{DR_G}{Dt} = -\zeta (R_G - R_{GEQ}). \quad (9)$$

The mean pressure is controlled to keep constant total volume.

3.3 Pressure equation

The procedure to solve the pressure field is analogous to the SMAC (Simplified-Marker-and-Cell) method. The equation for the pressure variation δp is expressed as,

$$\left[\nabla^2 - \frac{\zeta \rho_L f_{G0}}{(\Delta t)(1 + \zeta(\Delta t))p_0} \right] (\delta p) = \frac{\nabla \rho^{(N)} \cdot \mathbf{u}^* + \rho^{(N)} (\nabla \cdot \mathbf{u}^*)}{(\Delta t)} - \frac{3\rho_L f_{G0}}{R_{G0}} \frac{R_{G1}^{(*)} - R_{G1}^{(N)}}{(\Delta t)^2}. \quad (10)$$

The pressure, the bubble radius and the momentum are renewed using δp expressed as,

$$p^{(N+1)} = p^{(N)} + (\delta p), \quad R_{G1}^{(N+1)} = R_{G1}^{(*)} - \frac{(\Delta t)\zeta R_{G0}}{3(1 + \zeta(\Delta t))p_0} (\delta p), \quad (\rho \mathbf{u})^{(N+1)} = (\rho \mathbf{u})^{(*)} - (\Delta t) \nabla (\delta p). \quad (11)$$

3.4 Relaxation time of bubble radial motion

In order to formulate relaxation time of the bubble radial motion, the thermal viscosity of the gas bubble is considered under the assumption that the amplitude of bubble radial motion is small. According to Prosperetti *et al.* (1988), the effective viscosity μ_E is obtained from the perturbed equations of the Rayleigh-Plesset equation and the temperature inside the bubble and expressed as,

$$\mu_E = \mu + \mu_T \quad (12)$$

where μ_T is the thermal viscosity as a function of the gas pressure, the gas temperature, the bubble radius, the specific heat ratio and the heat transfer coefficient. ζ in Eq. (9) is expressed as,

$$\zeta = \frac{2\mu_E}{\rho_L R_{G0}}. \quad (13)$$

The relaxation time of the bubble radial motion is equal to $1/\zeta$.

3.5 Solution algorithm

The 4th-order finite difference method is employed to solve the partial differential equations. The discretization of variables is carried out on the staggered grid. The time integral is evaluated using the 2nd-order Adams-Bashforth method.

3.6 Simulation conditions

Before introducing the compressibility effect, a fully developed single-phase turbulent channel flow at the Reynolds number $Re_\tau (= \rho_L D u_\tau / \mu)$ of 150. The half width of the channel D , the friction velocity u_τ , the driving force H and the liquid density ρ_L are used to calculate dimensionless parameters and all of them are fixed to be 1 in the simulation. The dimensionless viscosity μ is $1/150$. The size of the simulation domain is set to $2\pi \times 2 \times \pi$ divided by $64 \times 64 \times 64$ grid points, in the streamwise (x), wall-normal (y) and spanwise (z) directions, respectively. The profiles of the mean velocity and the turbulent intensities obtained by the present simulation show good agreement with the DNS results by Kuroda *et al.* (1990) as shown in Fig. 6.

Parameters for the compressibility and the relaxation time of the bubble radial motion are equivalently given under the conditions that the bubbly liquid consists of air and water, the half width of the channel is 20mm, the flow velocity is 15m/s, the mean pressure is 100kPa, the void fraction is 10%, the bubble diameter is 0.5mm and the water temperature is 300K. From these conditions, the mean void fraction α_0 , the dimensionless static pressure p_0 and ζ are 0.1, 100 and 500, respectively. The flow direction is horizontal. In order to investigate the compressibility and the buoyancy effects, three simulations are performed as shown in Table 1.

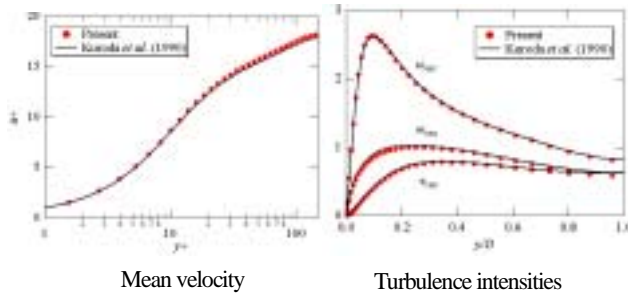


Fig. 6 DNS of single phase channel flow

Table 1 simulation conditions

	α_0	Fr
Case1	0	
Case2	0.1	
Case3	0.1	0.022

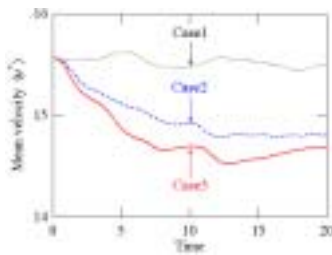


Fig. 7 Temporal evolution of mean flow rate

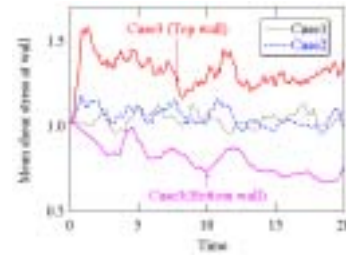


Fig. 8 temporal evolution of the mean shear stress

3.6 Results

Figure 7 shows the temporal evolution of the mean flow rate averaged over the simulation domain. The mean velocity without bubbles (case 1) is almost constant, while the mean velocities with bubbles (cases 2 and 3) decreases after introducing the bubbles at the time of 0. In the present study, the driving force and the viscosity are fixed so that such the decrease of the mean velocity indicates the increase of the friction drag on the wall. Figure 8 shows the temporal evolution of the mean shear stress averaged on the wall. The mean shear stresses without the buoyancy (case 1 and 2) is almost constant, while that with the buoyancy (case 3) decreases at the bottom wall and increases at the top wall after introducing the bubbles at the time of 0. In case 3, the void fraction near the top wall is higher than that near the bottom one due to the buoyancy. Therefore, the frictional drag near the higher void fraction region becomes higher.

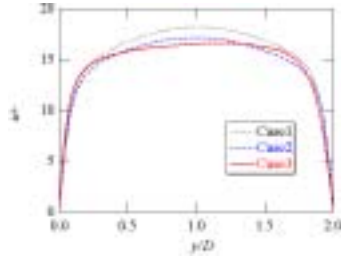


Fig. 9 Mean velocity profile

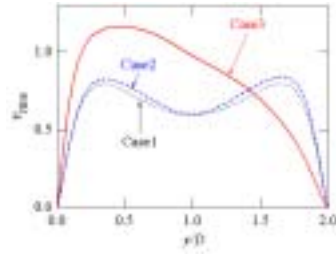


Fig. 10 Wall-normal rms velocity profile

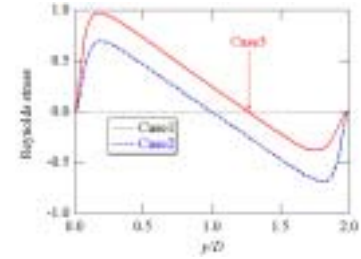


Fig. 11 $-\overline{\rho uv}$ profile

Figure 9, 10 and 11 show the profiles of the streamwise mean velocity \bar{u} , the wall-normal rms velocity v_{rms} and the Reynolds stress $-\overline{\rho uv}$, respectively. The sampling time for averaging is from 80 to 100. The positions y/D at 0 and 2 correspond to the top and bottom walls, respectively. It is seen from Figs. 10 and 11 that the turbulence intensities are augmented due to the compressibility of the bubbly liquid and stronger in the higher void fraction region. Such the turbulence augmentation decreases the mean velocity as shown in Fig. 9.

As mentioned above, the drag reduction is not observed in the present investigation on the bubble compressibility.

4. Effect of density fluctuation

The Direct Numerical Simulation (DNS) with much smaller grids than the bubble size is a powerful tool to obtain fine flow structures. However, a lot of numerical resources are consumed in the DNS and most of engineering simulations are unrealistic. Especially, the dense and sparse regions of bubbles are formed in the bubbly flow and such the density fluctuation often makes large flow structure beyond the computer capacity by the DNS. In order to investigate the effect of the density fluctuation, the two-fluid model based on the volume averaged equations, (Ishii, 1975; Drew, 1983; etc.) is useful. The conservation equations of the two-fluid model are directly derived from the Navier-Stokes (NS) equation, thus two-phase interaction due to the inertia difference may be adequately solved. On the other hand, equations for bubble motion are not derived from the NS equation. Constitutive equations for the bubble motion must be modeled in the two-fluid simulation. In this section, the model equation of the bubble motion is examined comparing with the experiment under the laminar flow condition.

4.1 Simulation method

The present simulation is based on the Eulerian-Lagrangian model developed by Murai and Matsumoto (1996). The mass and momentum equations are solved in the Eulerian way, while the equation of the bubble translational motion is solved in the Lagrangian way. The equation of the bubble translational motion involves the model equations of the forces on a bubble, e.g. drag and lift forces, etc. In the present study, the empirical formula of the drag coefficient C_D obtained by Schiller and Naumann (1933) is used and expressed as,

$$C_D = \frac{24}{Re_b} (1 + 0.15 Re_b^{0.687}), \quad (14)$$

where Re_b is the bubble Reynolds number ($Re_b = 2\rho_L |u_G - u_L| / \mu_L$). On the lift force F_L on a bubble, several model equations have been proposed. The lift force is expressed as,

$$\mathbf{F}_L = \frac{1}{2} \pi \rho_G^2 C_L \frac{|\mathbf{u}_G - \mathbf{u}_L|}{|\nabla \times \mathbf{u}_L|} (\mathbf{u}_G - \mathbf{u}_L) \times (\nabla \times \mathbf{u}_L), \quad (15)$$

where C_L is the lift force coefficient. Simulation conditions for C_L will be explained in Sec. 4.3.

4.2 Solution algorithm

The 4th-order finite difference method is employed to solve the partial differential equations. The discretization of variables is carried out on the staggered grid. The time integral of the flow velocity is evaluated using the 2nd-order Adams-Bashforth method. In terms of the time integral procedure of the translational motion of bubbles, 2nd-order Crank-Nicolson method and the 2nd-order Adams-Bashforth method are employed for the bubble position and the bubble velocity, respectively. The interpolation from the liquid phase to the gas one is approximated by the 5th-order Lagrangian interpolation. The local void fraction is calculated by the template-distribution model (Murai *et al.*, 2000).

4.3 Simulation conditions

The present simulation will be carried out under the same condition of the bubbly channel flow experiments performed by Kikugawa *et al.* (2001). They measured the mean velocity profile by the laser Doppler velocimetry. The flow direction is vertically upward. The half width of the channel D is 20mm. The Reynolds number Re ($=U_c D/\mu$) in the single phase flow is 950 and the flow is considered to be laminar. The liquid flow rate in the bubbly flow is same as that in the single phase flow. The mean void fraction (α_0) is 0.6%. The bubble diameter is 1mm.

The size of the simulation domain is set to 100mm \times 40mm \times 40mm divided by 50 \times 20 \times 20 grid points, in the streamwise (x), wall-normal (y) and spanwise (z) directions, respectively.

In the present study, we will examine following four C_L models.

Case 1 : No-lift

$$C_L^{(1)} = 0 \quad (16)$$

Case 2 : C_L for potential flow (Auton, 1987)

$$C_L^{(2)} = \frac{4}{3} \left(\frac{|\nabla \times \mathbf{u}_L| r_G}{|\mathbf{u}_G - \mathbf{u}_L|} \right) \quad (17)$$

Case 3 : Empirical C_L of a bubble (Sridhar and Katz, 1995)

$$C_L^{(3)} = 0.59 \left(\frac{|\nabla \times \mathbf{u}_L| r_G}{|\mathbf{u}_G - \mathbf{u}_L|} \right)^{0.25} \quad (18)$$

Case 4 : Numerical C_L of a rigid particle (Kurose and Komori, 1999)

$$C_L^{(4)} = C_L^{(4)} \left(\frac{|\nabla \times \mathbf{u}_L| r_G}{|\mathbf{u}_G - \mathbf{u}_L|}, \frac{r_G \Omega}{w |\mathbf{u}_G - \mathbf{u}_L|}, Re_b \right) \quad (19)$$

where Ω is the rotational angular speed and assumed to be equal to $|\nabla \times \mathbf{u}_L|/2$ in the present simulation. Using the data table shown by Kurose and Komori (1999), $C_L^{(4)}$ is estimated.

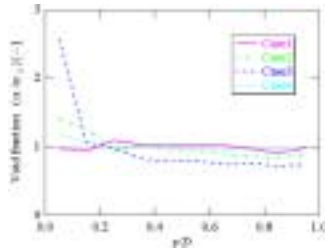


Fig. 12 Void fraction profile

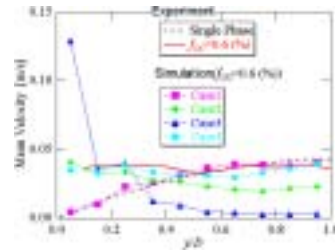


Fig. 13 Mean velocity profile

4.4 Results

Figure 12 shows the void fraction profile versus the length from the wall y/D for cases from 1 to 4. The bubble motion is affected by the lift force toward the wall due to the velocity gradient of the channel flow and the slip velocity of bubbles. As shown in Fig. 12, the void fraction near the wall becomes high except case 1 neglecting the lift force. The peak value of the void fraction strongly depends on the lift force model. It is experimentally known that the behavior of a bubble is markedly changed even by a very small amount of contaminant present in a liquid and that a small bubble in a contaminated liquid behaves similarly to a rigid sphere. Considering that the bubbles size in the experiment (Kikugawa *et al.*, 2001) is small enough to be treated as rigid spheres, C_L of case 3 or 4 is considered to be reasonable.

Figure 13 shows the mean velocity profile versus y/D . Lines without symbols correspond to the experimental results at the void fractions of 0 and 0.6%. Lines with symbols correspond to the present simulation result. Due to the buoyancy effect, the fluid in the higher void fraction region is driven upward. As shown in Fig. 13 that the mean velocity profile of case 1 almost agrees with the experimental result at the void fraction of 0%. It is because that the void fraction profile is almost independent of y/D (Fig. 12) and the effect of the local driving force due to the bubble buoyancy is weak. It is also seen from Fig. 13 that the mean velocity profile is sensitively affected by void fraction distribution. The simulation result with the lift fore model proposed by Kurose and Komori (1999), which is considered to be reasonable compared with experiment, shows the best agreement with the experiment.

5. DNS of channel flow with deforming bubbles

5.1 Numerical method

In this section, we present investigations of bubbly channel flow using a direct numerical simulation. Both liquid and gas phases are treated as incompressible fluids and solved by a finite volume method, while the interface between the phases is resolved by a front-tracking method specialized for treating deformed bubbles. A more detailed description of the method, and validations are found in the previous report (Kawamura and Kodama, 2001).

The size of bubbles that are used for the microbubble drag reduction is not small compared with the characteristic scale of turbulence. For example, the typical bubble size in the experiment of Takahashi et al.(2001) using a channel of 15 mm in height was 1mm, which is about 240 in the viscous unit. Therefore, we consider that application of the DNS is an effective way to investigate the influence of bubbles on turbulence.

Preliminary results of the DNS method were presented in the previous report , in which numerical simulations of a low Reynolds number bubbly channel flow were carried out. The results were found to be in qualitative agreement with experimental studies, while problems were that the ratio of the bubble diameter to the channel width was a factor of two to five larger than in the experiments. The difference in the size ratio is due to the limitation in the grid resolution. Since the DNS method resolves bubbles explicitly, the total number of the grid point depends on the size ratio between bubbles and computational domain. In the present study, a computation with a much finer resolution has been performed to simulate more realistic bubbly flow in a channel using a parallel computer.

5.2 Condition of simulation

A fully developed turbulent channel flow containing bubbles was investigated by the present numerical method. Before introducing the bubbles, a fully developed single-phase turbulent channel flow at the Reynolds number $Re_\tau=180$ based on the friction velocity u_τ a half width of the channel H , was computed. The size of the computational domain was set to $6.4H$, $3.2H$ and $2H$, in the streamwise, wall-normal and spanwise directions respectively. A periodic boundary condition was used in the streamwise and spanwise directions. The x -, y - and z - axes are taken in the streamwise, wall-normal and spanwise directions respectively. The number of the grid points was $256 \times 128 \times 128$. The computational domain was decomposed into four blocks in the streamwise direction, and each block of $64 \times 128 \times 128$ grid points was computed on a node of a parallel computer system. The number of the total grid points was 16 times more than in the previous study. At the nondimensional time $t^+ = u_\tau^2 t / \nu = 0$ bubbles were introduced at random locations. The bubble diameter was set to $0.2H$, and the number of bubbles was set to 98 bubbles. The mean void ratio in the computational domain was 1%. The Weber number based on the bulk mean velocity and the bubble diameter was 148.

5.3 Results

A snapshot of the distribution of bubbles is shown in Fig. 9 for comparing the size ratios among bubbles, the channel width and the scale of the streaky structure of near wall turbulence. The ratio of the bubble size to the channel width is 0.1, which is on the same order as in the experiments by Guin et al. (1996) and Takahashi et al. (1997), while the bubble diameter in the viscous unit is 36, which is about one third of the mean spacing between near wall streaks. Since the effect of the gravitational acceleration was not included in this DNS computation, the drift velocity between bubbles and liquid phase was very small.

Fig. 10 shows the profiles of the average void fraction over planes parallel to the walls at $t^+=0$ and a time-averaged value average from $t^+=100$ to $t^+=300$. Though the time-averaged profile still include some fluctuation, it is observed that the void fraction peaks at about $0.2H$ away from the walls. This is probably because of the momentum balance in the wall-normal direction. In a turbulent channel flow, the mean normal stress in the wall-normal direction $-\bar{p} - \rho \overline{v'v'}$ must be constant. Therefore the mean pressure \bar{p} is lowest where $\overline{v'v'}$ is highest. Bubbles are supposed to move to the low pressure region. The time evolution of the mean distance between bubbles and the wall shows that the bubbles are moving towards the walls on average. It is also noted that the bubble distribution has not reached statistical steady state.

The influence of the bubbles on the turbulence intensities are shown in Fig. 10. Though the time for averaging is not sufficient, the observed tendencies is that the intensities increase as a whole while the peak of the streamwise

intensity decreases. This tendency was the same in the previous study for larger bubbles. Fig. 11 shows one dimensional energy spectra of u' , v' and w' in the streamwise direction at $y^+=14$. The modulation of turbulence by bubbles is seen only in the high wave number region. This is consistent with the experimental observations (Serizawa et al., 1975). The Reynolds shear stress is slightly increased by bubbles as shown in Fig. 15, resulting in the slight increase in the friction coefficient shown in Fig. 16. This tendency was also the same in the previous study. This suggests the frictional drag is increased at low Reynolds numbers because of the additional dissipation around due to generation of vorticity around bubbles.

6. Conclusions

Various numerical simulation techniques were used to elucidate the mechanism of the microbubble drag reduction. The techniques can be grouped by the ways bubbles and turbulence are modeled. The macroscopic influence of bubbles through the decrease in the mean density and the increase in the effective viscosity can be simulated using the phase-averaged two-fluid model, moreover it has been shown that accurate profiles of void fraction and mean velocity in a laminar flow can be obtained by the proper choice of the lift force model.

For investigating the smaller scale interaction between bubbles and turbulence, the DNS methods, which resolve liquid phase flow and flow around bubbles in a single framework, should be used. DNS has been applied to a laminar two-dimensional Couette flow and a three-dimensional low Reynolds number turbulent channel flow in this study. It has been shown that the interactions between bubbles and laminar shear flow can be accurately computed, and a qualitative agreement has been confirmed in the turbulence modulation by bubbles.

The present investigations did not identify the origin of the microbubble drag reduction. However, it has been shown that the laminar interactions and the effect of compressibility of bubbles can not explain the decrease in the frictional drag. This suggests that the interaction between bubbles and turbulence is the source of the microbubble drag reduction. Although validations of the DNS method for turbulent flows are not thorough yet, the present study has shown that DNS of bubbly turbulent flow is possible by use of the present numerical methods. Further validation through quantitative comparisons with experiments, and extension to higher Reynolds number flows probably by introduction of sub-grid scale models are needed for elucidation of the phenomena.

References

- d'Agostino, L., d'Auria, F. and Brennen, C.E. (1997) *J. Fluid Mech.*, **339**, 261-274.
- Auton, T.R. (1987) *J. Fluid Mech.*, **197**, 241-257.
- Batchelor, G.K. (1967) *'An Introduction to Fluid Dynamics,'* (Cambridge University Press).
- Bogdevich, V.G., Evseev, A.R., Malyuga, A.G. and Migirenko, G.S. (1977) *Proc. of 2nd Int. Conf. on Drag Reduction*, **D2**, 25-36.
- Brennen, C.E. (1995) *'Cavitation and Bubble Dynamics,'* (Oxford University Press).
- Drew, D.A. (1983) *Annu. Rev. Fluid Mech.*, **15**, 261-291.
- Guin, M.M., Kato, H., Yamaguchi, H., Maeda, M. and Miyanaga, M. (1996) *J. Mar. Sci. Technol.*, **1**, 241-254.
- Ishii, M. (1975) *'Thermo-fluid Dynamics Theory of Two-phase Flow,'* (Eyrolles, Paris).
- Kikugawa, G., So, S., Takagi, S. and Matsumoto, Y. (2001) *Proc. of JSME FED*, 802 (CD-ROM) (in Japanese).
- Kawamura, T., Kodama, Y. (2001), *Proc. 2nd Symp. Turbulence and Shear Flow Phenomena, Stockholm, Sweden* (CD-ROM)
- Kodama, Y., Kakugawa, A., Takahashi, T. and Kawashima, H. (2000) *Int. J. Heat and Fluid Flow*, **21**, 582-588.
- Kuroda, A., Kasagi, N. and Hirata, M. (1990) *5th Symp. on Numerical Simulation of Turbulence, IIS of the Univ. of Tokyo*, 1-5.
- Kurose, R. and Komori, S. (1999) *J. Fluid Mech.*, **384**, 183-206.
- Legner, H.H. (1984) *Phys. Fluids.*, **27**, 2788-2790.
- Madavan, N.K., Deutsch, S. and Merkle, C.L. (1984) *Phys. Fluids.*, **27**, 356-363.
- Madavan, N.K., Merkle, C.L. and Deutsch, S. (1985) *Trans. ASME J. Fluids Eng.*, **107**, 370-377.
- Marié, J.L. (1987) *Int. J. Multiphase Flow*; **13**, 309-325.
- McCormick, M.E. and Bhattacharyya, R. (1973) *Naval Engineers J.*, **85**, 11-16.
- Murai, Y. and Matsumoto, Y. (1996) *Proc. of ASME FED*, **FED236**, 67-74.
- Murai, Y., Matsumoto, Y., Song, X.-Q., Yamamoto, F. (2000) *JSME Int. J. Ser. B* **43**, 180-187.
- Pal, S., Merkle, C.L. and Deutsch, S. (1988) *Phys. Fluids*, **31**, 744-751.
- Prosperetti, A., Crum, L.A., Commander, K.W. (1988) *J. Acoust. Soc. Am.*, **83**, 502-514.
- Schiller, L. and Naumann, A.Z. (1933) *Z. Ver. Dtsch. Ing.*, **77**, 318-320.
- Sridhar, G. and Katz, J. (1995) *Phys. Fluids*, **7**, 389-399.
- Serizawa, A., Kataoka, I. and Michiyoshi, I. (1975) *Int. J. Multiphase Flow*, **2**, 235-246
- Sugiyama, K., Takagi, S. and Matsumoto, Y. (2001) *Comput. Methods Appl. Mech. Engrg.*, **191**, 689-704.
- Takahashi, T., Kakugawa, A. and Kodama, Y. (1997) *J. Soc. Naval Archit. Jpn.*, **182**, 1-8 (in Japanese).
- Yoshida, Y., Takahashi, Y., Kato, H., Masuko, A. and Watanabe, O. (1997) *J. Mar. Sci. Technol.*, **2**, 1-11.

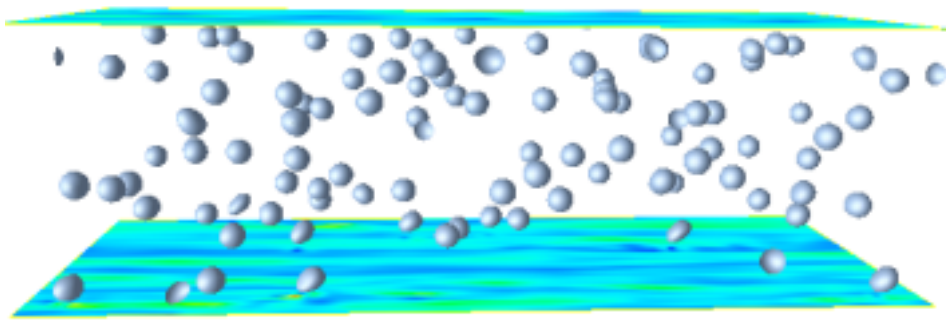


Fig. 9 Snapshot of bubble distribution at $t^+=200$ in the DNS of bubbly channel flow ($Re_\tau=180, \alpha=1\%$). Colors on indicate the streamwise component of the instantaneous wall shear stress.

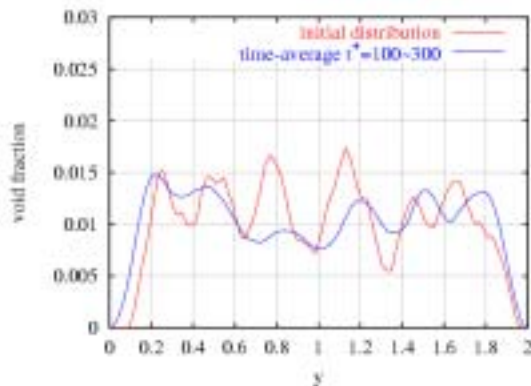


Fig. 10 Void fraction profiles in the DNS of bubbly channel flow ($Re_\tau=180, \alpha=1\%$).

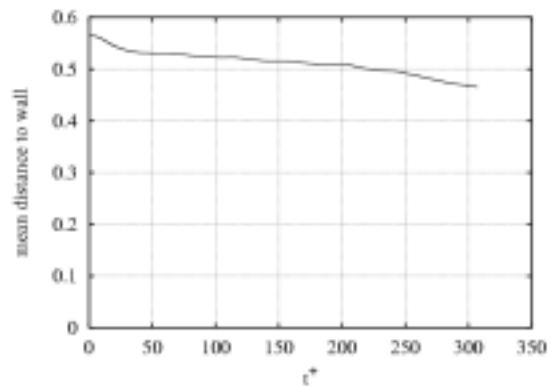


Fig. 11 Time evolution of the mean distance between bubbles and the wall in the DNS of bubbly channel flow ($Re_\tau=180, \alpha=1\%$).

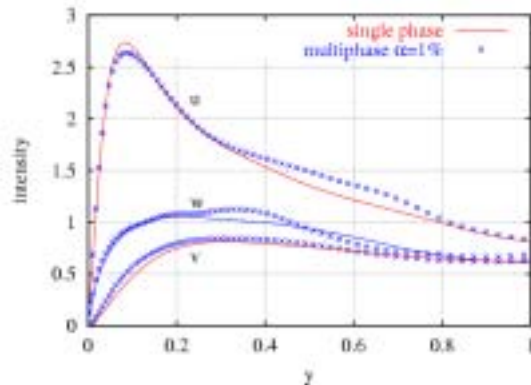


Fig. 12 Turbulence intensity profiles in the DNS of bubbly channel flow ($Re_\tau=180, \alpha=1\%$).

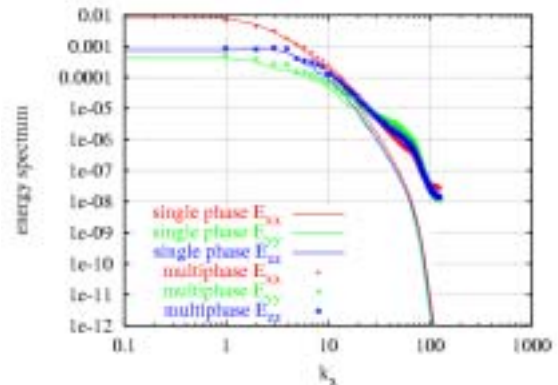


Fig. 14 One-dimensional energy spectra at $y=14$ in the DNS of bubbly channel flow ($Re_\tau=180, \alpha=1\%$).

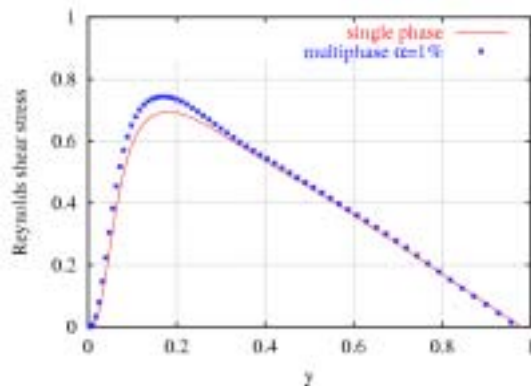


Fig. 15 Profiles of the Reynolds shear in the DNS of bubbly channel flow ($Re_\tau=180, \alpha=1\%$).

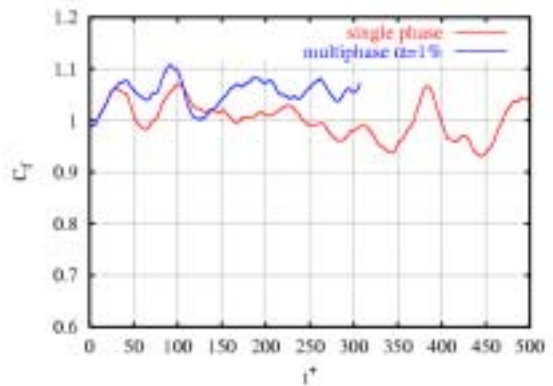


Fig. 16 Time histories of the normalized frictional drag coefficient in the DNS of bubbly channel flow ($Re_\tau=180, \alpha=1\%$).